On-Orbit Performance of the GF-7 Satellite Laser Altimetry System from 2020 to 2024

Jun Peng[1], Guoyuan Li[1,2] , Jiyi Chen[2], Aiyan Guo[3]

[1] Shandong University of Science and Technology, Qingdao, Shandong, China - 3234479326@qq.com; ligy_lasac@foxmail.com
[2] Land Satellite Remote Sensing Application Center, Ministry of Natural Resources, Beijing, China - chenjy@lasac.cn
[3] China Academy of Space Technology, Beijing, China - guoaiyan@126.com

Keywords: GF-7 Satellite, Laser Altimeter, Performance Evaluation, Full waveform.

Abstract

The Gaofen-7 (GF-7) satellite represents China's first civil satellite equipped with a full waveform laser altimeter. This study aims to evaluate its on-orbit performance by analyzing the transmitting and receiving systems through the examination of waveform parameter and laser energy. The results indicate that the transmitting waveform of Beam 1 exhibits a little instability compared to that of Beam 2. It is supposed that the extreme solar activity on March 31st, 2022, affected the stability of the receiving waveform of Beam 1 in April 2022, while simultaneously impacting the stability of transmitting waveform and the receiving waveform of Beam 2’s transmitting and receiving. As a result, the pulse width of the receiving waveform for both Beams has been extended by approximately 1.5 ns and 2.4 ns, respectively after April 2022. Both beams have experienced a decline in ability to emit laser energy, with Beam 1 decreasing by 0.4 mJ per month and Beam 2 by 0.08 mJ per month. Notably, following the extreme solar activity, the rate of decline became more pronounced, escalating to 0.5 mJ per month for Beam 2. Overall, Beam 1 demonstrated superior transmitting and receiving radiation capacity compared with Beam 2, while the receiving radiation performance of both beams remained relatively stable. Nevertheless, there were some changes in the full waveform data transmitted and received by the altimetry system during the four years on-orbit peroid of the GF-7 satellite, the changes were very small, highlighting the overall stability of the laser altimetry system.

1. Introduction

LiDAR, as an active imaging system, provides high-precision distance measurements that are not affected by lighting conditions, in contrast to passive imaging systems. Furthermore, when compared to microwave imaging systems, LiDAR exhibits superior angular resolution, measurement accuracy, and resistance to interference, while also being more amenable to miniaturization (Liu et al., 2019). Since the beginning of the new century, satellite laser altimetry has undergone significant developments. NASA launched the ICESat satellite in 2003, followed by ICESat-2 (Neumann et al., 2019) and GEDI (Dubayah et al., 2020) in 2018. In China, ZY3-02 was launched in 2016 (Li et al., 2019), which was equipped with the first satellite laser altimeter for Earth observation. After that, China subsequently launched the GF-7 (Zhang et al., 2020), ZY3-03 (Li et al., 2022), and GF-14 (Cao et al., 2023) and the terrestrial ecosystem carbon inventory satellite (CM-1) (He et al., 2022), all of which carried a satellite laser altimetry system.

The ICESat satellite encountered an operational issue when Laser 1 ceased functioning 38 days post-launch due to manufacturing defects in its semi-conductor laser tube pumping array. Consequently, it was designed to operate intermittently, with three cycles of 33 days each year to fulfill its follow-up mission (Wang et al., 2011). Anthony et al. (2023) analyzed four years of transmitted laser pulse energy data from ICESat-2, revealing a gradual overall decline in the transmitter's laser energy of approximately 1% to 2%. Furthermore, their analysis of photon point cloud data from the Antarctic region indicated that the receiver's signal sensitivity declines at an annual rate of 2.6%. Based on these studies, they upgraded the laser emission energy level from 4 to 5 and predicted that the ATLAS system could maintain its current performance through the end of the 2030s.

The experimental laser altimetry payload on the ZY3-02 satellite has completed its operational lifespan so after launch. During the mission, it collected data from over 100 orbits. This data was valuable for joint stereo mapping validation that integrate laser altimetry data with optical remote sensing imagery, effectively meeting the project's objectives (Li et al., 2017).

The GF-7 satellite was successfully launched on November 3, 2019. It was equipped with a laser altimeter that contained four lasers (two main lasers and two spare lasers), with only two lasers operating simultaneously. The specific parameters of the laser altimetry system are detailed in Table 1. The altimeter achieves a ranging accuracy of better than 0.3 meters on flat terrain and is primarily employed for obtaining global elevation control points for stereo mapping at a scale of 1:10,000(Tang et al., 2022; Meng et al., 2020). Although the laser altimetry system of the GF-7 satellite has been working on orbit for over four years and has reached half of its expected operational lifespan, its on-orbit hardware performance has not yet been evaluated. This study aims to evaluate the hardware performance of the laser altimetry system aboard the GF-7 satellite. The assessment utilizes transmit and receiving waveform data collected over four years, focusing on key parameters such as waveform pulse width, amplitude, skewness, kurtosis, background noise threshold, and waveform signal-to-noise ratio. The results will guide subsequent on-orbit missions of GF-7, and provide a reference for GF-7 data processing and the design of domestic satellite laser altimetry payloads.

Parameter	Value
Pulse Width	5-8 ns
Number of Beams	2
Repetition Frequency	3 Hz
Laser Wavelength	1064 nm
Pulse Energy	90-180 mJ
Footprint Size	<25m

Table 1 Nominal values of the main parameters of the GF-7 altimeter instrument

2. On-Orbit Evaluation Method for the GF-7 Satellite Laser System

This study mainly uses waveform pulse width, amplitude, skewness, kurtosis, background noise standard deviation, and

waveform signal-to-noise ratio to evaluate the received waveform and receiving waveform, to evaluate the hardware performance of the receiving system and the transmitting system.

2.1 Amplitude and Pulse Width of Waveform

For laser altimeters, both the transmitting and receiving waveforms can be considered Gaussian, and the peak and pulse width parameters of the corresponding waveforms can be obtained by fitting the Gaussian function.

$$y = Ae^{-\frac{(x-\mu)^2}{2\sigma^2}} \tag{1}$$

where A = the amplitude of the corresponding fitted waveform
δ = the standard deviation of the fitted waveform
μ = the mean value of the fitted waveform

2.2 Skewness, Kurtosis of Waveform

Skewness and kurtosis are used to evaluate the degree of deviation of waveform data from the standard normal distribution, which can be expressed as follows:

$$SK = \frac{\sum_{i=1}^{n}(w_i - \overline{w})^3}{(n-1)\sigma_n^3} \tag{2}$$

$$K = \frac{1}{(n\text{-}1)\ \sigma_n^4}\sum_{i=1}^{n}(w_i - \overline{w})^4 \tag{3}$$

where SK = skewness of the waveform
K = kurtosis of the waveform
w_i= intensity value of the waveform at the corresponding sampling position
$\overline{w}$ = sample average of the waveform
δ_n = sample standard deviation of the waveform
n = the number of samples

Skewness serves as a measure to assess the symmetry of the data distribution. A skewness value less than zero indicates a left-skewed distribution, whereas a value greater than zero indicates a right-skewed distribution. The kurtosis of a standard normal distribution is defined as 3. When the kurtosis value is less than 3, the data distribution is considered flatter than that of the standard normal distribution; conversely, when the kurtosis exceeds 3, the data distribution is regarded as sharper than that of the standard normal distribution.

2.3 Background Noise Threshold and Signal-to-Noise Ratio

The background noise threshold of the transmitted waveform and the waveform signal-to-noise ratio can be expressed by the following equations (6) and (7) respectively.

$$\sigma_n = \sqrt{\frac{1}{k}\sum_{i=1}^{k}(w_i - \overline{w})^2} \tag{4}$$

$$\mu_n = \frac{1}{k}\sum_{i=1}^{k} w_i \tag{5}$$

$$B = \mu_n + N\sigma_{noise} \tag{6}$$

$$SNR_w = 10\lg\frac{w_{\max} - B}{\sigma_n} \tag{7}$$

where δ_{noise} = the background noise standard deviation
μ_n = the background noise average
k = the number of samples
B = the background noise threshold
N= the background noise standard deviation of a multiple of this paper according to the empirical value of 4
SNR_w = signal-to-noise of the waveform
w_{max} = the maximum intensity of the waveform

3. Results and Analysis

In this study, we utilize the transmitting and receiving waveform data derived from the GF-7 Level 1 product. Each month, data from 200 orbits were randomly selected, and over a duration exceeding four years, from March 2020 to June 2024, we extracted skewness, kurtosis, and pulse width of the transmitting waveforms based on the aforementioned evaluation metrics to analyze the deformation of transmitting waveforms within a long-term series. Additionally, we extracted background noise thresholds, signal-to-noise ratio parameters, and laser energy parameters directly obtained from the Level 1 products to assess the emitted radiation performance of the transmitting system, resulting in the extraction of approximately tens of thousands of related single parameters monthly. Acknowledging that environmental conditions, such as terrain features and atmospheric conditions, significantly influence the evaluation indices of the receiving system, this paper incorporates supplementary information, including ground feature type, cloud cover, surface slope, and surface roughness. This information is employed to randomly select track numbers that meet the criteria outlined in Section 3.2 for extracting relevant parameters from the received data. Due to insufficient data availability in 2020, which resulted in a lack of statistical significance, this analysis is confined to the evaluation indicators of the receiving system derived over three and a half years, from January 2021 to June 2024, with approximately thousands of valid data points screened each month.

3.1 Transmitting System Performance Evaluation

Parameters such as skewness, kurtosis, and pulse width are effective indicators of variations in the waveform. The background noise threshold, emitted laser energy, and signal-to-noise ratio of the waveform enable a comprehensive analysis of the system's radiation performance, considering both background radiation and laser emitted radiation. The subsequent analysis will concentrate on the deformation of the emitted waveform by evaluating data about skewness, kurtosis, and pulse width. Furthermore, the alterations in the radiation characteristics of the transmitting system will be examined based on data that includes the amplitude of the waveform, emitted laser energy, background noise thresholds, and signal-to-noise ratios of the waveform.

3.1.1 Transmitting Waveform Changes

Figures 1 and 2 illustrate the monthly variations in skewness and kurtosis of the emission waveforms.
Both Beams exhibit skewness values consistently less than 0 and very close to 0 over the four years. The kurtosis values are approximately 2 and remain below 3, indicating relatively stable changes, with corresponding variances of less than 1e-4. Notably, the kurtosis of Beam 1 has increased, while Beam 2 experienced a large increase in April 2022. These observations suggest that the pulse shape of the GF-7 emission is left-skewed compared to the standard Gaussian waveform.

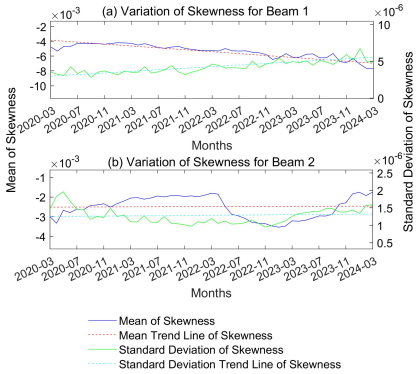

Figure 1 Monthly variation of the skewness of the transmitting waveform

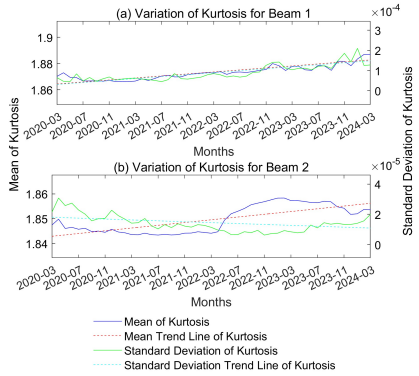

Figure 2 Monthly variation of the kurtosis of the transmitting waveform

Figure 3 illustrates the monthly variations in pulse width of the transmit waveforms. For Beam 1, the pulse width has decreased at a rate of approximately 0.036 ns per month. In contrast, Beam 2 exhibited relative stability until April 2022, after which there was a noticeable upward trend, although the overall change remains small at about 0.003 ns per month.

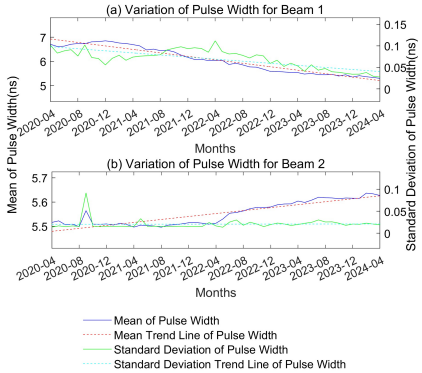

Figure 3 Monthly variation of the pulse width of the transmitting waveform

The monthly variations in skewness, kurtosis, and pulse width for the transmit waveforms of Beam 1 show greater variance compared to Beam 2. This indicates that the transmit pulse shape for Beam 1 is more unstable.

3.1.2 Transmitting Radiation Changes

Figure 4 presents the monthly variations in emitted laser energy.

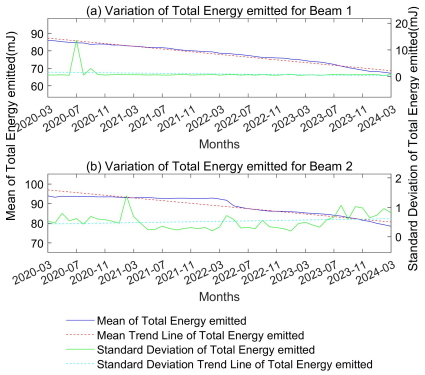

Figure 4 Monthly variation of the Emitted laser energy of the transmitting waveform

The emitted laser energy for Beam 1 has shown a declining trend over time, despite an increase in the amplitude of the emitted laser energy. Beam 2 remained relatively stable at around 92 mJ for most months leading up to April 2022. However, in May 2022, the emitted laser energy of Beam 2 has been a significant drop to 88 mJ, and it has gradually decreased month by month since then. The amplitude of the emitted laser waveform closely mirrors the changes in the amplitude of the emitted energy. Before April 2022, changes in laser energy were gradual, followed by a increase that peaked in January 2023, after which there was a some decline, with a slight rebound noted in December 2023.

In summary, both beams exhibit a decline in their laser energy emission capabilities, with Beam 1 decreasing at a rate of 0.4 mJ per month, while Beam 2 has declined at rates of 0.08 mJ per month before April 2022 and 0.5 mJ per month afterward.

Despite the decrease in energy for both Beams, Figure 5 indicates that the amplitude of the transmitting waveform had increased. For Beam 1, this increase can be attributed to a combination of higher kurtosis and reduced pulse width. While the overall emitted energy had decreased, the heightened kurtosis and narrower pulse width mean that the laser energy was more concentrated around the peak during a time, resulting in a higher amplitude. For Beam 2, the primary factor influencing the increase in amplitude was the change in kurtosis, as its pulse width has remained relatively stable(Fig. 3), and the amplitude of the emitted laser (as in Fig. 5) is consistent with the change in the kurtosis of the pulse shape of Beam 2 (as in Fig. 2).

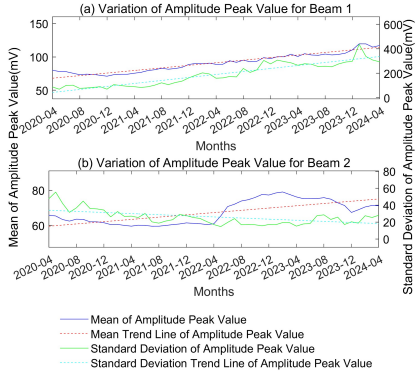

Figure 5 Monthly variation of the amplitude of the transmitting waveform

Figures 6 and 7 illustrate the monthly variations in the signal-to-noise ratio (SNR) of the transmitting waveforms and the

background noise thresholds for both beams. Notably, the SNR for both Beams has increased, while their background noise thresholds have decreased.

Beam 1 shows a slightly better SNR, approximately 20.5 dB, compared to Beam 2’s 18.5 dB. Additionally, the background noise threshold for Beam 1 is marginally lower at around 89.2 mV, while Beam 2 measures about 90 mV. These phenomena indicate that the instrumental transmitting radiation performance of Beam 1 is slightly better than that of Beam 2.

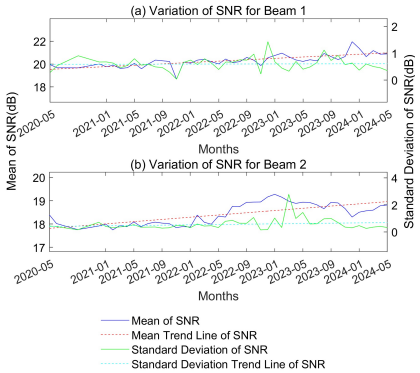

Figure 6 Monthly variation of the signal-to-noise ratio of the transmitting waveform

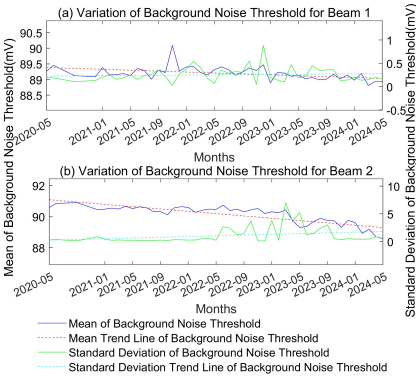

Figure 7 Monthly variation of the background noise threshold of the transmitting waveform

3.2 Receiving System Reception Performance Evaluation

To mitigate the influences of varied terrains and features, data corresponding to bare ground were selected, utilizing the feature types provided by Global Land30, the cloud cover parameter from the GF-7 laser footprint image, and the receiving saturation parameter from the SLA03 product. The selection criteria were as follows: feature type classified as desert, surface roughness less than 1, slope less than 1, surface cloud cover below 10%, and an SLA03 saturation parameter *m_Wf_Saturation*=0 (indicating unsaturation). From this filtered dataset, 200 tracks meeting these criteria were randomly chosen to extract relevant parameters.

According to Dengnan (2002), the primary radiation received by the receiving system comprises laser signal reflected from the surface, solar background radiation, and background noise generated by the electrical noise within the receiver instrument. The signal is predominantly influenced by surface reflectivity, while the received waveform is affected by terrain characteristics and the instrumentation system, including factors such as divergence angle, pointing angle, and the spreading effect due to waveform sampling. Studies conducted by Ji and Zou (1994) and Cao et al. (2014) indicate that reflectance and solar radiation in desert regions gradually decrease around June (marking the onset of the rainy season and summer), while these parameters increase near December (during the dry season and winter).

While the previously mentioned conditions contribute to the mitigation of the effects of terrain, features, and atmospheric conditions, seasonal variations in surface reflectance and solar radiation remain insufficiently addressed. The skewness and kurtosis of the received waveform are significantly influenced by environmental factors, whereas the primary determinants of the received pulse width are the transmit pulse width and the terrain conditions. Consequently, the subsequent section primarily focuses on utilizing variations in the receiving pulse width to assess changes in the received waveform. Given that the terrain screening conditions are consistent, metrics such as background noise threshold, amplitude, and signal-to-noise ratio can be employed to evaluate the relative performance of the two beams in terms of radiation reception.

3.2.1 Receiving Waveform Changes

Figure 8 illustrates the monthly variations in the pulse width of the receiving waveforms.

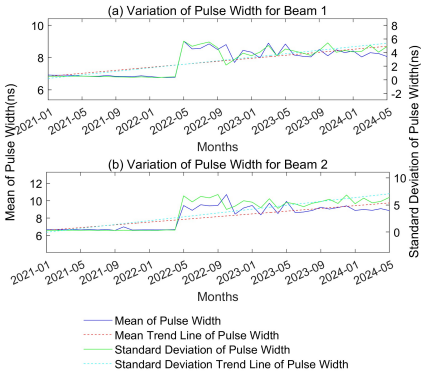

Figure 8 Monthly variation of the pulse width of the receiving waveform

Before April 2022, the pulse width of the Beam 1 receiving waveform was consistently around 6.8 ns, while the Beam 2 receiving waveform averaged approximately 6.7 ns until April 2022. Subsequently, there was a increase somewhat in pulse width to 8.3 ns for Beam 1 and 9.0 ns for Beam 2. This change suggests that the implemented screening conditions effectively mitigated the impacts of terrain and atmospheric factors.

Synthesizing the analysis in section 3.1.1 suggests that the stability of the receiving waveform in the Beam 1 receiving system was adversely affected by specific elements in April 2022. Simultaneously, the stability of both the receiving and transmitting waveforms in the Beam 2 system experienced comparable disruptions. This occurrence increased the pulse width of the receiving waveforms, measuring approximately 1.5 ns for the Beam 1 receiving system and 2.4 ns for the Beam 2 receiving system, respectively.

3.2.2 Receiving Radiation Changes

Figures 9, 10, and 11 present the monthly variations in the amplitude, background noise threshold, and waveform signal-to-noise ratio of the receiving waveforms.

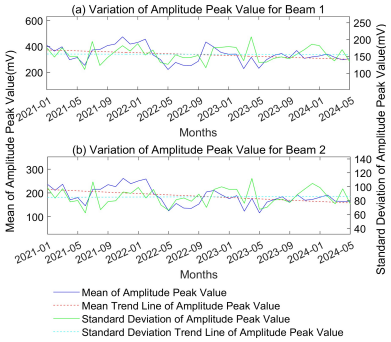

Figure 9 Monthly variation of the amplitude of the receiving waveform

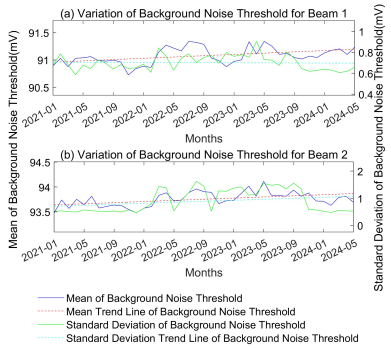

Figure 10. Monthly variation of the background noise threshold of the receiving waveform

The data indicate that the amplitude and waveform SNR of Beam 1 is consistently higher than those of Beam 2, while the background noise threshold for Beam 1 is lower. This aligns with the findings from the transmitted waveforms, as both Beams can be considered observations made under identical conditions. Thus, it suggests that the receiving radiation performance of the Beam 1 system surpasses that of Beam 2.

The trends of the receiving waveform amplitude and waveform SNR are similar with a decreasing trend near June and an increasing trend near December, respectively. According to the analysis in Section 3.2, the changes of these two parameters may be caused by the surface reflectivity. On the other hand, the trend of background noise threshold is opposite, and the change of this parameter is likely to be caused by solar radiation. These parameters oscillated near June and December, respectively, but were always within a range, indicating that the relevant parameters were maintained at a relatively stable level with little variation, and that the radiation performance of the receiving system instrumentation remained in a relatively stable state.

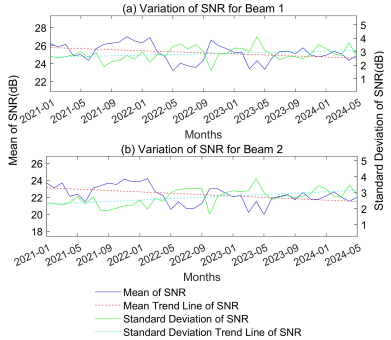

Figure 11. Monthly variation of the signal-to-noise ratio of the receiving waveform

3.2.3 GF-7 SLA03 Accuracy

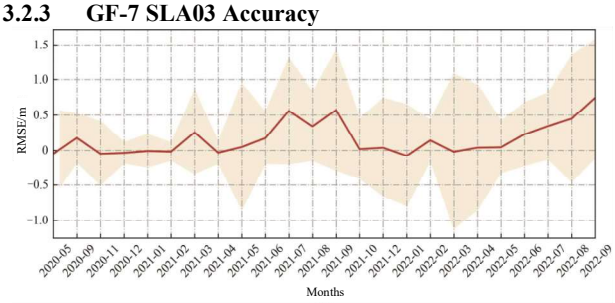

Figure 12 The monthly variation trends of terrain height errors(Cited from Chen et al.,2024)

GF-7 altimetry data mainly provide elevation control points for optical image stereo mapping. The author's team analyzed in detail the accuracy of GF-7 in altimetry in another document as shown in Figure 12. It can be seen that the long-time sequence accuracy of SLA03, the laser standard product of GF-7, is stable. In the plain area, the RMSE of elevation accuracy reaches 0.653 m, and more than 60% of the accuracy is better than 0.3 m(RMSE). The result shows that 60% of the SLA03 data can provide elevation control points for 1:10,000 scale stereo mapping in the plain area.

3.3 Analysis of Contributing Factors

The results presented above suggest that around April 2022, the satellite platform experienced an event that compromised the stability of the altimeter system. According to Zhou et al. (2012), charged particles in space radiation can cause radiation damage to spacecraft materials, microelectronic devices, optical windows, temperature control and other instruments, and is currently one of the important causes of spacecraft anomalies and failures on orbit. While the space radiation environment is significantly influenced by fluctuations in solar activity during the 11-year solar cycle (Hajipour et al., 2013). Notably, the year 2022 corresponds to the 25th solar cycle, and the observed decline in the stability of the GF-7 altimeter system during April 2022 is likely attributable to an increase in space radiation into this solar cycle. The F10.7 index, which measures solar radio flux at a wavelength of 10.7 cm, serves as an indicator of solar radiation energy injection. To assess whether the satellite was impacted by solar activity in April 2022, this study collected F10.7 index data for the period from March 2022 to May 2022 from the Helmholtz Centre Potsdam website (https://kp.gfz-potsdam.de/en/data). The findings, illustrated in Figure 13, reveal that the F10.7 index reached a peak of 239 on March 31, 2022. According to the Australian Space Weather Prediction Centre (https://www.sws.bom.gov.au/Educational/1/2/4), an F10.7 index exceeding 196 is indicative of extreme solar activity. This suggests that the extreme solar activity observed on March 31, 2022 likely had a detrimental effect on the stability of the satellite's altimetry following April 2022.

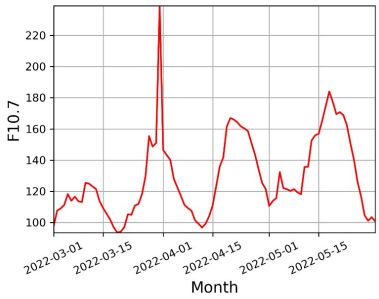

Figure 13. F10.7 Index daily change, March 2022-May 2022

4. Summary

This study mainly evaluates the laser height measurement transmitting system and receiving system of GF-7 satellite through waveform skewness, amplitude, pulse width, background noise threshold, and signal-to-noise ratio, et cetera. The conclusions include:

1) It is supposed that the extreme solar activity on March 31st, 2022, adversely affected the stability of the receiving and transmitting waveforms of the Beam 2 system in April 2022. Additionally, the stability of the receiving waveform of the Beam 1 receiving system also experienced a decline. As a result of the effect, the receiving waveforms of the Beam 1 and Beam 2 systems widened by approximately 1.5 ns and 2.4 ns, respectively.

2) The ability of both beams to emitted laser energy has decreased. Beam 1 maintains a decrease of 0.4mJ/month, and Beam 2 decreases by 0.08mJ/month and 0.5mJ/month before and after the extreme solar activity. Overall, Beam 1 has a stronger ability to transmitting and receiving radiation compared to Beam 2.

The results show that GF-7 as the first China's satellite to carry a dual-beam laser altimeter payload, the measurement quality of the two beams has been very stable during the four years on orbit, showing the great progress of China's aerospace hardware manufacturing. The results of this paper can provide important guidance for the future on-orbit missions of GF-7 and offer a reference for GF-7 data processing and the design of domestic satellite laser altimeter payloads.

Acknowledgements

The paper is supported by the Civil Space pre-Research Project (Grant No. D030104), the National Key Research and Development Program of China (Grant No. 2022YFB3903603) and the National Natural Science Foundation of China (Grant No. 41971425).

References

Abshire, J. B., Sun, X., et al., 2005. Geoscience Laser Altimeter System (GLAS) on the ICESat Mission: Initial science measurement performance. Geophysical Research Letters, 32, L21S02.

Cao, B., Wang, J., Hu, Y., et al., 2023. On-orbit geometric calibration and preliminary accuracy verification of the GaoFen-14 laser measurement system. Optics and Precision Engineering, 31(11): 1631-1640.

Cao, B., Yang, X., Yue, C. 2014. Spatiotemporal analysis of surface reflectance in Xinjiang region. Forestry Survey and Planning, 39(04): 5-9.

Chen J Y， Tang X M， Li G Y， Liu Z and Zhou X Q. 2024. Terrain height assessment of satellite laser altimetry standard products for natural resources. National Remote Sensing Bulletin， 28（3）：704-716 DOI：10.11834/jrs.20233021.

Degnan, J. J. 2002. Photon-counting multikilohertz microlaser altimeters for airborne and spaceborne topographic measurements. Journal of Geodynamics, 34(3-4): 503-549.

Fei, Z., Qiang, L., Tailin, X., et al., 2012. Analyses and countermeasures of in-orbit satellite failures caused by pace radiation environment. Spacecraft Environmental Engineering, 29(4): 392-396.

Hajipour, P., Danaeefar, M., Ebrahimzadeh, M., et al., 2013: Space environment and evaluation of typical high altitude satellites. Journal of Iranian Association of Electrical and Electronics Engineers, 10(2), 49-56.

He, T., Guo, A., Huang, J., et al., 2022. Overview of the land ecosystem carbon monitoring satellite "Jumang". International Space, (09): 8-12.

Ji, G., Zou, J. 1994. Seasonal variations of radiation balance in oases and deserts in arid regions. Plateau Meteorology, (03): 100-106.

Li, G., Gao, X., Chen, J., et al., 2019. Quality analysis of laser altimetry data from Ziyuan-3 02 satellite. *Journal of Remote Sensing*, 23(06): 1159-1166.

Li, G., Tang, X. 2017. Precision analysis and validation of laser altimetry from Ziyuan-3 02 satellite. Journal of Surveying and Mapping, 46(12): 1939-1949.

Li, G., Tang, X., Zhou, P., et al., 2022. Processing and integrated mapping applications of laser altimetry data from the Ziyuan-3 03 satellite. Infrared and Laser Engineering, 51(05): 441-449.

Liu, B., Yu, Y. Jiang, S., 2019. Advances in LiDAR detection and 3D imaging research. Optoelectronic Engineering, 46(07): 21-33.

Martino, A. J., Cavanaugh, J., Gibbons, A., et al., 2023. ICESat-2/ATLAS at 4 years: Instrument performance and projected life. In Advanced Photon Counting Techniques XVII (Vol. 12512, pp. 47-61). SPIE.

Meng, J., Zhang, X., Jiang, J., et al., 2020. Design of the laser for the GaoFen-7 satellite laser altimeter. Spacecraft Engineering, 29(03): 96-102.

Neumann, T. A., et al., 2019. The Ice, Cloud, and Land Elevation Satellite–2 Mission: A global geolocated photon product derived from the advanced topographic laser altimeter system. *Remote Sensing of Environment*, 233, 111325.

Tang, X., Wang, H. 2022. Establishment and application of the civil optical satellite surveying product system in China. Journal of Surveying and Mapping, 51(07): 1386-1397.

Wang, C., Li, X., Peng, H. 2015. Simulation analysis technology of onboard full-waveform laser altimeter. Progress in Laser and Optoelectronics, 52(10): 102801.

Wang, X., Cheng, X., Gong, P., et al., 2011. Earth science applications of ICESat/GLAS: A review. International Journal of Remote Sensing, 32(23): 8837-8864.

Zhang, X., He, T., Zhao, C., et al., 2020. Surveying system and performance evaluation of the GaoFen-7 satellite. Spacecraft Engineering, 29(03): 1-11.